

Evaluation of stress intensity factors under thermal effect employing domain integral method and ordinary state based peridynamic theory

Hanlin Wang^a, Satoyuki Tanaka^{a*}, Selda Oterkus^b, Erkan Oterkus^b

^a Graduate School of Advanced Science and Engineering, Hiroshima University, Japan

^b Department of Naval Architecture, Ocean and Marine Engineering, University of Strathclyde, United Kingdom

Abstract In this article, several thermoelastic benchmark cases are studied within the framework of ordinary state based peridynamic theory (OSPD). By using OSPD, the limitations of geometrical discontinuity in fracture analysis can be overcome. Meanwhile, double nodes can also be avoided during crack definition. A domain integral method with thermal effect is applied in calculating the thermal stress intensity factors (TSIFs). Meanwhile, peridynamic differential operators (PDDO) are utilized to rewrite the spatial derivatives in the domain integral. Numerical investigations of TSIFs in the single and mixed-mode crack scenarios are provided respectively, and verified by the reference solutions. Good agreements between OSPD and the reference solutions show high performance and capability of the proposed method in thermoelastic fracture analysis.

Keyword Ordinary state based peridynamics · Peridynamic differential operator · Interaction integral · Thermoelastic fracture analysis · Thermal stress intensity factor.

Nomenclature

A	Area enclosed by contours Γ_0, Γ and crack surfaces	$f(\mathbf{x}_i), f(\mathbf{x}_j)$	Arbitrary physical parameters on points \mathbf{x}_i and \mathbf{x}_j
a	Crack length		
A_0	Area enclosed by contour Γ_0 and crack surfaces	f_I, f_{II}	Functions for analytical solutions of crack tip stress field on mode-I and -II
a_1, a_2, a_3, b, d	OSPD parameters		
$A_{(n_1 n_2)(q_1 q_2)}$	PD shape matrix		
$a_{q_1 q_2}^{p_1 p_2}$	Unknown coefficient matrix	g_I, g_{II}	Functions for analytical solutions of crack tip displacement field on mode-I and -II
b_i	Body force density of point i		
$b_{n_1 n_2}^{p_1 p_2}$	Known coefficient matrix	$g_2^{p_1 p_2}$	2D PD function
c_v	Specific heat capacity	H	Thickness of plate
E, E^*	Elastic modulus	H_x	Horizon of point x
		J	J-integral or J value

J^s	J-integral by superimposing states	W_F	Thermoelastic strain energy density
k	Thermal conductivity	W_i	Strain energy density of point i
K_I, K_{II}	Mode-I and -II SIFs		
K_I^*, K_{II}^*	Normalized mode-I and -II SIFs	w_{ij}	Weight function for equation of motion in OSPD
L	Length of a 2D structure		
\tilde{L}	Lagrangian	x, y	Global coordinates
$m(x, t)$	Bond connection indicator of point x at time t	x', y' $\mathbf{x}_i, \mathbf{x}_j$	Local coordinates Initial configuration of points i and j
M	Interaction integral		
N	Total number of material points in numerical model	$\mathbf{y}_i, \mathbf{y}_j$	Deformed configuration of points i and j
n	Total number of material points in the horizon	A	Coefficient of thermal expansion
q, q_j	q -function and its spatial derivatives in M	Γ, Γ_0	Outer and inner J-integral contour
R	Remainder terms in Taylor Series	Δ δ_{ij}	Horizon size Kronecker delta
R_0	Region for q equals to 1	ε_{ij}	Strain components
R_1	Region for linearly decrease of q from 1 to 0	Δx Θ	Grid space Angle between horizontal axis and bond
r	Distance from crack tip		
r_d	Size of integral contour	Θ_i	Dilatation term of point i
s_{ij}	Bond stretch	K	Bulk modulus
\tilde{T}	Kinetic energies	$\tilde{\kappa}$	Micro thermal conductivity
$T_i(t), T_i$	Temperature of point i at time t	λ_L	Lamé's constant
$\dot{T}_i(t), \dot{T}_i$	Time derivative of temperature of point i at time t	M μ_L	Shear modulus Lamé's constant (shear modulus)
$T_{i,1}$	Spatial derivative of temperature on x' direction	N ξ_1, ξ_2	Poisson's ratio x and y components of bond
t_{ij}	Force state of point i		
\tilde{U}	Potential energies	P	Mass density
\mathbf{u}_i	Displacement component of point i	σ_{ij} T	Cauchy stress components Temperature difference between pairwise points of bond
$\dot{\mathbf{u}}_i, \ddot{\mathbf{u}}_i$	First and second order time derivatives of \mathbf{u}_i		
$u_{i,1}$	Spatial derivative of \mathbf{u}_i on x' direction	Φ	Angle from horizontal axis
V_i	Volume of point i	$\Phi_i(x, t)$	Damage value of point i on position x at time t
W	Width of a 2D structure	Ψ	Crack inclined angle

$\omega_{q_1 q_2}$ Weight function for
PDDO

Abbreviation

ADR	Adaptive dynamic relaxation	PD	Peridynamics
BBPD	Bond based peridynamics	PDDO	Peridynamic differential operator
CCM	Classical continuum mechanics	PDEs	Partial differential equations
CTE	Coefficient of thermal expansion	SIFs	Stress intensity factors
FEM	Finite element method	TSIFs	Thermal stress intensity factors
OSPD	Ordinary state based peridynamics		

Superscript

aux Auxiliary field

1 Introduction

Fracture analysis is one of the most cutting-edge research topics including complex physical behaviors in solid mechanics. Cracks, usually as an inevitable phenomenon in physics, are commonly existed in almost all materials and structures in the world. Unstable crack growth and propagation might lead to failure of local and global structural integrity. In many engineering applications, such as solid oxide fuel cell, LNG tank and internal combustion chamber, structures are always accompanied with extreme temperatures during operation. Therefore, thermal effects can play significant roles in fracture phenomenon, which requires tremendous attention on them.

Many efforts are devoted to the investigation of damage and failure. Irwin [1] proposed an analytical method in solving the stress concentration level in the vicinity of the crack tip. He found that the stress values in this region can be expressed by a scaled factor, which is known as stress intensity factors (SIFs). However, the stress state around the crack tip is complex and it will bring mathematical difficulties for the determination of stress and strain fields. Therefore, Rice [2] introduced a path-independent method to approximate the strain/stress concentration at crack tip regions, named as J-integral (or J value). By appropriately defining the integral contour, strain energy release rate can be calculated, and then the SIF can be determined as $K = \sqrt{J \cdot E}$, where E is an elastic modulus and J represents J-integral value. Without direct evaluation, the difficulties of SIF calculation can be overcome and the accuracy can be assured.

Based on classical continuum mechanics (CCM), various numerical simulation methods are developed for SIF evaluation. Chen et al. [3] proposed a Lagrangian finite difference method (FDM) in the fracture analysis of central cracked plate. The dynamic SIF at the vicinity of crack tip is discussed and summarized in detail. Based on J-integral, Yau et al. [4] and Stern et al. [5] developed an interaction integral in calculating the mixed-mode SIFs for two-dimensional (2D) pre-damaged plates. By processing the composition of the actual field and auxiliary field, mode-I and -II SIFs can be extracted separately. Yu et al. [6] and Song et al. [7] further applied the interaction integral on non-homogeneous material. Kim et al. [8] used the interaction integral on the fracture analysis of functional graded materials. The interaction integral is also widely employed in thermoelastic fracture mechanics. Zamani et al. [9] and Duflo [10] analyzed mixed-mode TSIFs by using extended FEM. Besides, Nguyen et al. [11] studied the thermoelastic benchmark problems by using extended nodal gradient FEM. Various types of crack modes are elaborately discussed in terms of static and dynamic TSIFs. Moreover, Hosseini-Tehrani et al. [12] applied the boundary element method (BEM) to calculate dynamic mode-I SIF. These numerical methods have proved the strong applicability and reliability of the interaction integral in both mechanical and thermoelastic fracture analysis.

In CCM, the deformation of structures or particles is described by partial differential equations (PDEs), and the geometrical continuity is strongly required [13]. However, fracture and failure are geometrically discontinuous in their nature. It will bring

difficulties for tracking the crack evolution, and the re-meshing process is unavoidable during numerical simulation, which will consume a large amount of computing resources [14]. Hence, for the analysis of dynamic fracture behavior, various techniques are developed, such as cohesive zone method (CZM) [15, 16]. However, CZM experiences dependency problem due to the alignment of cohesive elements on element boundaries. Therefore, extended finite element method (XFEM) is employed to overcome this limitation. Even though allowing the crack propagation within elements, the detection of the crack surface in 3D modelling is a challenging problem for XFEM. Phase field method is also popular in the evaluation of dynamic fracture mechanics [17]. Since this method is governed by higher order PDEs in primal form, it might have difficulties in solving problems with complicated geometries [18]. On the other hand, meshfree methods are developed to overcome the limitations of CCM in fracture analysis. Tanaka et al. [19] introduced a meshfree Galerkin method in the investigation of 2D in-plane fracture mechanics problem. Based on stabilized conforming nodal integration (SCNI), this meshfree method has shown excellent reliability and accuracy in calculating of mixed-mode SIFs. The SCNI is further employed and validated on the fracture analysis of Mindlin-Reissner plate [20, 21]. Meanwhile, Pant et al. [22] also studied the thermoelastic problems by applying the meshfree Galerkin method.

Nonlocal theory and higher-gradient continuum mechanics have been introduced by Gabrio Piola more than 100 years ago [23], but they become popular in recent decades. Peridynamic theory (PD), as an alternative nonlocal meshfree method, was first introduced by Silling [24] and it has many applications in fracture analysis. Imachi et al. [25] employed the OSPD in the analysis of mixed-mode 2D fracture problems. Good agreements between OSPD solutions and reference solutions in terms of dynamic SIFs indicate the OSPD has strong capability in fracture mechanics. Dai et al. [26, 27] further utilized the PDDO in fracture analysis of flat shell structure by OSPD. By using PDDO, the PDEs can be replaced by spatial integral equations, which makes the interaction integral embed into the OSPD framework properly. The PD has also taken the deformation under thermal effect into consideration. Oterkus et al. [28] had applied the bond based peridynamic theory (BBPD) in simulating the thermal diffusion and coupled field thermoelastic deformation. Later on, Madenci et al. [29] used OSPD to investigate of thermoviscoelastic deformation and fracture evolution. Nguyen et al. [30] applied OSPD to investigate the thermoelastic behaviors of shell structures. Ren et al. [31] improved the PD by introducing the dual horizon. The dual horizon PD has shown a better calculating efficiency and good performance in multi-material fracture analysis. Based on FEM, Dorduncu et al. [32] had developed a truss element for PD. Comparing with the traditional PD, it requires much fewer computing efforts before failure. Based on integro-differential equations, PD is straightforward to deal with discontinuities with good accuracy and efficiency. Within the framework of PD, PPDO can transform the PDEs into spatial integral equations. Although there are some other techniques available for the same purpose such as smoothed particle hydrodynamics (SPH), reproducing kernel particle method (RKPM), etc., PDDO is a robust technique and has similar characteristics as traditional PD.

To the best of authors' knowledge, the studies about thermoelastic fracture analysis by using interaction integral under the framework of OSPD are rare. Therefore, in this article, TSIFs are evaluated by calculating several classical benchmark problems, and results by OSPD will be validated by reference solutions.

The paper is structured as follows: In the second section of this article, the fundamental knowledge about OSPD will be presented, and the 2D PDDO will be illustrated in the third section. In the fourth section, the expression of thermoelastic interaction integral will be provided and the numerical benchmark problems will be discussed in the fifth section. In the final section, the numerical method and results will be briefly summarized.

2 Ordinary state based peridynamic theory

PD, later named as BBPD, was first introduced by Silling [24] as an extension of solid mechanics. In this theory, structure is discretized by finite number material points with a certain volume. Each point can interact with all surrounding points within finite distance and the collection of these points is called "Horizon" (H_x) as shown in Fig. 1. The interaction between each pair of these points is named as "bond". It is assumed that bonds can only exist within the horizon. The influence from points outside the horizon are so weak that can be ignored. Bonds may deform as structure deforms, which gives rise to the pairwise forces as shown in Fig. 1. However, the BBPD is oversimplified and it has many limitations in numerical simulation. For example, the Poisson's ratio has to be 1/3 and 1/4 for 2D and 3D problems, respectively. Therefore, Silling et al. [33] had further developed the constitutive model and proposed the OSPD. By redefining material-dependent parameter and introducing the concept of "state", the limitations in BBPD had been overcome.

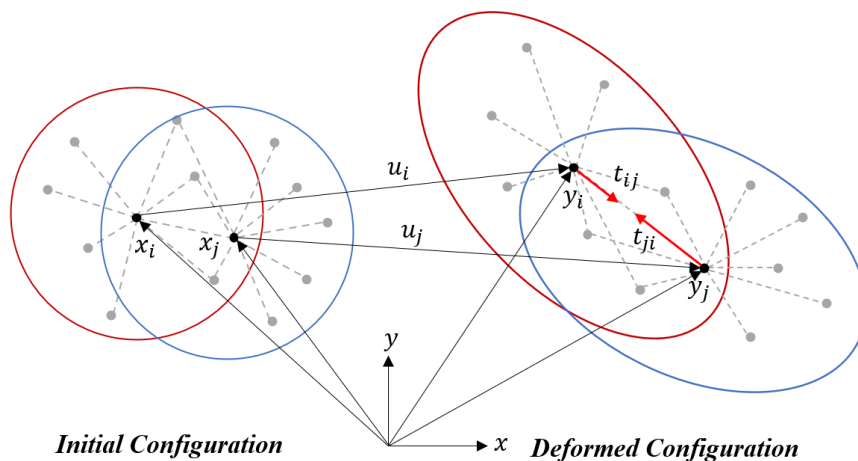


Fig. 1 Horizon and pairwise force

2.1 Equation of motion

Equation of motion could be derived from principle of virtual work by solving the Lagrange's equation [34], which is shown as:

$$\frac{d}{dt} \left(\frac{\partial \tilde{L}}{\partial \dot{\mathbf{u}}_i} \right) - \frac{\partial \tilde{L}}{\partial \mathbf{u}_i} = 0, \quad (1)$$

with

$$\tilde{L} = \tilde{T} - \tilde{U}, \quad (2)$$

where \mathbf{u}_i and $\dot{\mathbf{u}}_i$ refer to the displacement components and the time derivate of displacement components of point i , respectively. Lagrangian \tilde{L} is defined as shown in Eq. (2), where \tilde{T} and \tilde{U} are total kinetic and potential energies respectively, which can be expressed as:

$$\tilde{T} = \sum_{i=1}^N \frac{1}{2} \rho \dot{\mathbf{u}}_i \dot{\mathbf{u}}_i V_i, \quad (3)$$

$$\tilde{U} = \sum_{i=1}^N W_i V_i - \sum_{i=1}^N \mathbf{b}_i \mathbf{u}_i V_i, \quad (4)$$

where W_i is the strain energy density of point i . N is the total number of material points in the solution domain. \mathbf{b}_i and V_i are body force density and volume of point i , respectively. Substituting Eqs. (2)-(4) back to Eq. (1), the numerical expression of equation of motion of OSPD can be expressed as:

$$\rho \ddot{\mathbf{u}}_i = \sum_{j=1}^n [\mathbf{t}_{ij} - \mathbf{t}_{ji}] V_j + \mathbf{b}_i, \quad (5)$$

$$t_{ij} = \frac{1}{V_j} \frac{\partial W_i}{\partial (|\mathbf{y}_j - \mathbf{y}_i|)} \frac{\mathbf{y}_j - \mathbf{y}_i}{|\mathbf{y}_j - \mathbf{y}_i|}, \quad (6)$$

where n represents the total number of material points in the horizon. Note that, even though the force states \mathbf{t}_{ij} and \mathbf{t}_{ji} are similar in expression, they are not the same in physical meaning, because they are determined by the material points in their own horizons. In OSPD by considering thermal effects, W_i can be expressed as:

$$\begin{aligned} W_i = & a_1 \Theta_i^2 - a_2 \Theta_i T_i(t) + a_3 (T_i(t))^2 \\ & + b \sum_{j=1}^n w_{ij} \{ (|\mathbf{y}_j - \mathbf{y}_i| - |\mathbf{x}_j - \mathbf{x}_i|) - \alpha T_i(t) |\mathbf{x}_j - \mathbf{x}_i| \}^2 V_j, \end{aligned} \quad (7)$$

where $T_i(t)$ is the temperature of point i at time t and α is the coefficient of thermal expansion (CTE). For 2D cases, the dilatation term Θ_i can be expressed as:

$$\Theta_i = d \sum_{j=1}^n w_{ij} \left(s_{ij} - \alpha T_i(t) \right) \frac{\mathbf{y}_j - \mathbf{y}_i}{|\mathbf{y}_j - \mathbf{y}_i|} \cdot (\mathbf{x}_j - \mathbf{x}_i) V_j + 2\alpha T_i(t). \quad (8)$$

The PD parameters a_1 , a_2 , a_3 , b and d in Eqs. (7) and (8) can be represented as [34]:

$$a_1 = \frac{1}{2} (\kappa - 2\mu), a_2 = 4\alpha a_1, a_3 = 4\alpha^2 a_1, b = \frac{6\mu}{\pi h \delta^4}, d = \frac{2}{\pi h \delta^3}, \quad (9)$$

where κ is bulk modulus and μ is shear modulus, h is the thickness of the 2D structure and δ is the size of horizon.

Usually, the shape of horizon is line, circle and sphere for 1D, 2D and 3D problems, respectively. Therefore, the member points within the horizon may not always have full volume especially for the points located on the boundary of the horizon. Hence, a volume correction factor, varies from 0 to 1, is employed for each material to represent the real volume enclosed by the horizon. Meanwhile, some material points might not have a full-size horizon, since they are close to the structure boundaries. Therefore, it will lead to a decrease on both local and global stiffness of the structure. Hence, by comparing with CCM, a surface correction factor is applied to OSPD formulation to minimize the surface effect.

2.2 Damage

Bond may elongate or shorten during the structural deformation. Once the bond stretch exceeds a critical value, bond will irreversibly break as shown in Fig. 2. Usually, a parameter m is applied to indicate the situation of bond connection. $m(x, t) = 1$ indicates normal bond and $m(x, t) = 0$ for broken bond. Therefore, in PD, damage of a material point generally refers to the percentage of broken bond in its horizon, which can be represented as:

$$\Phi_i(x, t) = \frac{\int_{H_x} m(x, t) dV}{\int_{H_x} dV}. \quad (10)$$

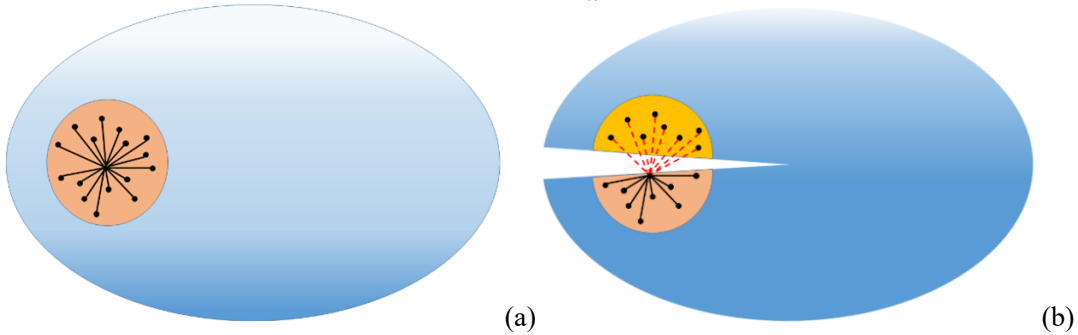


Fig. 2 Damage occurrence: (a) before damage, (b) after damage

3 Peridynamic differential operator

Generally, most kind of physical phenomena, such as thermal conduction, ion diffusion and mechanical deformation can be described by PDEs. In specific cases, they are too complicated to be solved by analytical methods. Thanks to the development of computing technologies, numerical methods, such as FEM [35], FDM [36] and BEM [37] are widely applied in approximating the PDEs. As mentioned previously, these methods have difficulties in fracture analysis due to discontinuous property of the solution domain. Meanwhile, a large amount computing resources are necessary for numerical solution [38]. Madenci et al. [39] proposed the PDDO to approximate the PDEs within the framework of PD. By using PDDO, PDEs are replaced by spatial integral equations, which overcomes the geometry discontinuity problem during

fracture analysis [40, 41]. In this article, 2D PDDO will be presented.

PDDO can be derived from Taylor's Series. The 2D Taylor's Series can be expressed as:

$$\begin{aligned} f(\mathbf{x}_j) = f(\mathbf{x}_i) &+ \xi_1 \frac{\partial f(\mathbf{x}_i)}{\partial x} + \xi_2 \frac{\partial f(\mathbf{x}_i)}{\partial y} \\ &+ \frac{1}{2!} \xi_1^2 \frac{\partial^2 f(\mathbf{x}_i)}{\partial x^2} + \frac{1}{2!} \xi_2^2 \frac{\partial^2 f(\mathbf{x}_i)}{\partial y^2} + \xi_1 \xi_2 \frac{\partial^2 f(\mathbf{x}_i)}{\partial x \partial y} + R, \end{aligned} \quad (11)$$

where $f(\mathbf{x}_i)$ and $f(\mathbf{x}_j)$ can be any physical parameter of material point i and j , respectively. ξ_1 and ξ_2 refer to the x and y component of the bond vector ξ , respectively. R , as remainder terms, are assumed small enough to be neglected. Moving the first term on the right-hand side to the left, and multiplying each term with PD function ($g_2^{p_1 p_2}(\xi)$) and integrating through the horizon, Eq. (11) can be reformulated as:

$$\begin{aligned} \int_{H_x} (f(\mathbf{x}_j) - f(\mathbf{x}_i)) g_2^{p_1 p_2}(\xi) dV &= \frac{\partial f(\mathbf{x}_i)}{\partial x} \int_{H_x} \xi_1 g_2^{p_1 p_2}(\xi) dV \\ &+ \frac{\partial f(\mathbf{x}_i)}{\partial y} \int_{H_x} \xi_2 g_2^{p_1 p_2}(\xi) dV + \frac{\partial^2 f(\mathbf{x}_i)}{\partial x^2} \int_{H_x} \frac{1}{2!} \xi_1^2 g_2^{p_1 p_2}(\xi) dV \\ &+ \frac{\partial^2 f(\mathbf{x}_i)}{\partial y^2} \int_{H_x} \frac{1}{2!} \xi_2^2 g_2^{p_1 p_2}(\xi) dV + \frac{\partial^2 f(\mathbf{x}_i)}{\partial x \partial y} \int_{H_x} \xi_1 \xi_2 g_2^{p_1 p_2}(\xi) dV, \end{aligned} \quad (12)$$

where $p_1, p_2 = 0, 1, 2$ except $p_1 = p_2 = 0$. In current 2D second order integrations, the horizon size is defined as three times of the grid size. Invoking the orthogonality property of PD function yields:

$$\frac{1}{n_1! n_2!} \int_{H_x} \xi_1^{n_1} \xi_2^{n_2} g_2^{p_1 p_2}(\xi) dV = \delta_{n_1 p_1} \delta_{n_2 p_2} \text{ with } n_1, n_2 = 0, 1, 2, \quad (13)$$

where δ_{np} is Kronecker delta. Substituting Eq. (13) into Eq. (12), the relationship between PDEs and PD functions can be expressed as:

$$\begin{pmatrix} \frac{\partial f(\mathbf{x}_i)}{\partial x} \\ \frac{\partial f(\mathbf{x}_i)}{\partial y} \\ \frac{\partial^2 f(\mathbf{x}_i)}{\partial x^2} \\ \frac{\partial^2 f(\mathbf{x}_i)}{\partial y^2} \\ \frac{\partial^2 f(\mathbf{x}_i)}{\partial x \partial y} \end{pmatrix} = \int_{H_x} (f(\mathbf{x}_j) - f(\mathbf{x}_i)) \begin{pmatrix} g_2^{10}(\xi) \\ g_2^{01}(\xi) \\ g_2^{20}(\xi) \\ g_2^{02}(\xi) \\ g_2^{11}(\xi) \end{pmatrix} dV. \quad (14)$$

The 2D PD functions, $g_2^{p_1 p_2}(\xi)$, are composed of weight function ω and elements of

unknown matrix $a_{q_1 q_2}^{p_1 p_2}$ as:

$$g_2^{p_1 p_2}(\xi) = a_{10}^{p_1 p_2} \omega_{10} \xi_1 + a_{01}^{p_1 p_2} \omega_{01} \xi_2 + a_{20}^{p_1 p_2} \omega_{20} \xi_1^2 + a_{02}^{p_1 p_2} \omega_{02} \xi_2^2 + a_{11}^{p_1 p_2} \omega_{11} \xi_1 \xi_2. \quad (15)$$

The unknown coefficient matrix $a_{q_1 q_2}^{p_1 p_2}$ depends on PD shape matrix $A_{(n_1 n_2)(q_1 q_2)}$

and known coefficient matrix $b_{n_1 n_2}^{p_1 p_2}$, which can be expressed as:

$$\sum_{q_1=0}^2 \sum_{q_2=0}^{2-q_1} A_{(n_1 n_2)(q_1 q_2)} a_{q_1 q_2}^{p_1 p_2} = b_{n_1 n_2}^{p_1 p_2}. \quad (16)$$

Matrix $A_{(n_1 n_2)(q_1 q_2)}$ depends on a weight function ω and initial bond vector ξ . The relationship between these factors can be represented as:

$$A_{(n_1 n_2)(q_1 q_2)} = \int_{H_x} \omega_{q_1 q_2} \xi_1^{n_1+p_1} \xi_2^{n_2+p_2} dV. \quad (17)$$

The known coefficient matrix $b_{n_1 n_2}^{p_1 p_2}$ can be constructed as:

$$b_{n_1 n_2}^{p_1 p_2} = n_1! n_2! \delta_{n_1 p_1} \delta_{n_2 p_2}. \quad (18)$$

Weight function is a manually defined function to represent the influence of interaction between material points. Usually, the larger in distance, the less in influence. Therefore, in this study, weight function is defined as:

$$\omega_{q_1 q_2} = \left(\frac{\delta}{|\xi|} \right)^{q_1+q_2+1}. \quad (19)$$

Substituting, Eqs. (17)-(19) back to Eq. (16), the unknown coefficient matrix $a_{q_1 q_2}^{p_1 p_2}$ can be calculated as:

$$a_{q_1 q_2}^{p_1 p_2} = \begin{bmatrix} \frac{2}{\pi h \delta^4} & 0 & 0 & 0 & 0 \\ 0 & \frac{2}{\pi h \delta^4} & 0 & 0 & 0 \\ 0 & 0 & \frac{9}{\pi h \delta^6} & -\frac{3}{\pi h \delta^6} & 0 \\ 0 & 0 & -\frac{3}{\pi h \delta^6} & \frac{9}{\pi h \delta^6} & 0 \\ 0 & 0 & 0 & 0 & \frac{12}{\pi h \delta^6} \end{bmatrix}. \quad (20)$$

Therefore, according to Eq. (15), 2D PD can be calculated as:

$$g_2^{10}(\xi) = \frac{2}{\pi h |\xi| \delta^2} \cos \theta, \quad (21a)$$

$$g_2^{01}(\xi) = \frac{2}{\pi h |\xi| \delta^2} \sin \theta, \quad (21b)$$

$$g_2^{20}(\xi) = \frac{9}{\pi h |\xi| \delta^3} \cos^2 \theta - \frac{3}{\pi h |\xi| \delta^3} \sin^2 \theta, \quad (21c)$$

$$g_2^{02}(\xi) = -\frac{3}{\pi h |\xi| \delta^3} \cos^2 \theta + \frac{9}{\pi h |\xi| \delta^3} \sin^2 \theta, \quad (21d)$$

$$g_2^{11}(\xi) = \frac{12}{\pi h |\xi| \delta^3} \cos \theta \sin \theta, \quad (21e)$$

where θ is the angle between bond and horizontal axis. Substituting Eqs. (21) in Eq. (14), the integral form of 2D PDEs in both first order and second order can be calculated. Meanwhile, the 1D and 3D PD function can be found in [39, 42, 43].

4 Thermal stress intensity factor

4.1 Interaction integral by taking thermal effect into account

According to Irwin's theory [1], SIFs, as important fracture characteristic parameters, represent the stress concentration states in the vicinity of crack tips in linear elastic fracture mechanics. Based on the theory proposed by Wilson and Yu [44], for homogeneous material and static situations, the domain integral with consideration of thermal effect can be expressed as:

$$J = \int_A (\sigma_{ij} u_{i,1} - W_F \delta_{1j}) q_{,j} dA + \beta \int_A \varepsilon_{ii} T_{i,1} q dA + \beta \int_{A_0} \varepsilon_{ii} T_{i,1} dA. \quad (22)$$

As shown in Fig. 3, local coordinate x' and y' is defined on crack tip. A is area enclosed by contours Γ_0 , Γ and crack surfaces. A_0 is area enclosed by contours Γ_0 and crack surfaces. As A_0 is shrinking to the crack tip, the third term on the right-hand side of Eq. (22) can be ignored. $u_{i,1}$ and $T_{i,1}$ are spatial derivatives of displacement vector and temperature in x' direction, respectively. δ_{ij} is Kronecker delta. Based on [45], the strain energy density can be represented by considering thermal effects as:

$$W_F = \frac{1}{2} \sigma_{ij} \varepsilon_{ij} - \frac{\beta}{2} T_i(t) \varepsilon_{ii}, \quad (23)$$

where ε_{ij} is elastic strains and σ_{ij} is corresponding to Cauchy stress which can be expressed as:

$$\sigma_{ij} = \frac{\partial W_F}{\partial \varepsilon_{ij}} = 2\mu_L \varepsilon_{ij} + \lambda_L \varepsilon_{kk} \delta_{ij} - \beta T_i(t) \delta_{ij}, \quad (24)$$

where μ_L and λ_L are Lamé's constants. The parameter β can be expressed as:

$$\beta = \begin{cases} \frac{E\alpha}{1-\nu} & \text{plane stress} \\ \frac{E\alpha}{1-2\nu} & \text{plane strain} \end{cases}, \quad (25)$$

where E is elastic modulus; ν is Poisson's ratio and α is coefficient of thermal expansion.

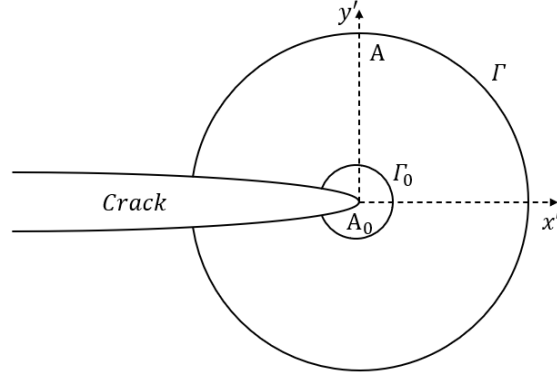


Fig. 3 J-integral contour at the crack tip region

By superimposing the actual and auxiliary fields of Eq. (22), the interaction integral can be formulated. The superimposing domain integral (denoted as J^S) can be expressed as:

$$J^S = \int_A \{(\sigma_{ij} + \sigma_{ij}^{aux})(u_{i,1} + u_{i,1}^{aux}) - (W_F + W_F^{aux})\delta_{1j}\} q_{,j} dA \quad (26)$$

$$+ \beta \int_A (\varepsilon_{ii} + \varepsilon_{ii}^{aux})(T_{i,1} + T_{i,1}^{aux}) q dA,$$

where q is manually defined weight function. Usually, it varies from 0 at contour edge to 1 at crack tip. In this study, q can be explained by frustum shape model as shown in Fig. 4. Within the region R_0 , q equals to 1. Within the region R_1 , q value experiences a linear decrease from 1 on inner boundaries to 0 on the outer boundaries of R_1 , as shown in Eq. (27). $q_{,j}$ refer to the spatial derivatives of q function on local coordinates x' and y' .

$$q = \begin{cases} 1 & \text{within } R_0 \\ (0, 1) & \text{within } R_1 \\ 0 & \text{outside } R_1 \end{cases} \quad (27)$$

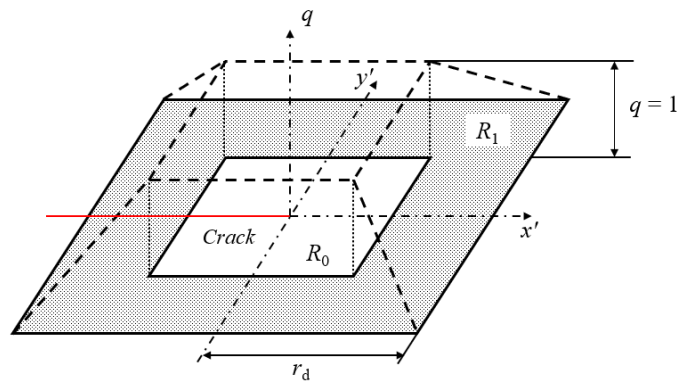


Fig. 4 Description of q distribution surrounding a crack tip

By decomposing Eq. (26), the interaction integral can be expressed by actual field J and auxiliary field J^{aux} domain integrals as:

$$M = J^S - J - J^{aux}, \quad (28a)$$

$$M = \int_A (\sigma_{ij}^{aux} u_{i,1} + \sigma_{ij} u_{i,1}^{aux} - \sigma_{ik} \varepsilon_{ik}^{aux} \delta_{1j}) q_{,j} dA + \int_A [\beta \varepsilon_{kk}^{aux} T_{i,1}] q dA. \quad (28b)$$

The auxiliary stress fields and displacement fields are distributed as shown in Fig. 5 [46] and they can be expressed as:

$$\sigma_{ij}^{aux} = K_I^{aux} f_I(r, \phi) + K_{II}^{aux} f_{II}(r, \phi), \quad (29a)$$

$$u_i^{aux} = K_I^{aux} g_I(r, \phi) + K_{II}^{aux} g_{II}(r, \phi), \quad (29b)$$

where r and ϕ are coordinates in polar coordinate system. The expression of parameter $f_I(r, \phi)$, $f_{II}(r, \phi)$, $g_I(r, \phi)$ and $g_{II}(r, \phi)$ can be found in many studies in the literature, such as [46]. Recalling Eq. (14), the derivatives in Eq. (28b) can be replaced by integral equation with respect to horizon, which has built up the relationship between the domain integral and OSPD.

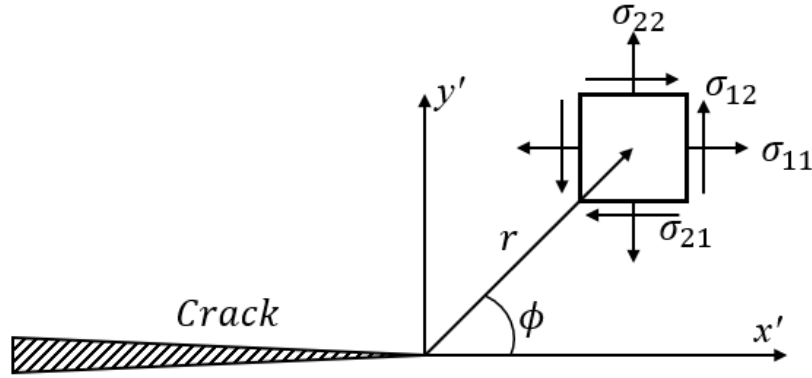


Fig. 5 Auxiliary stress distribution at the vicinity of the crack tip

The relationship between domain integral and TSIFs under mixed-mode can be expressed as:

$$J^S = \frac{(K_I + K_I^{aux})^2 + (K_{II} + K_{II}^{aux})^2}{E^*}, \quad (30)$$

where $E^* = E$ for plane stress assumption and $E^* = E/(1 - \nu^2)$ for plane strain assumption. Substituting Eq. (30) into Eq. (28a), the interaction integral can also be expressed in terms of TSIFs as:

$$M = \frac{2}{E^*} (K_I K_I^{aux} + K_{II} K_{II}^{aux}). \quad (31)$$

By selecting particular auxiliary modes, the mode-I and -II TSIFs can be extracted respectively, as:

$$K_I = \frac{E^*}{2} M \quad (K_I^{aux} = 1, K_{II}^{aux} = 0), \quad (32a)$$

$$K_{II} = \frac{E^*}{2} M \quad (K_I^{aux} = 0, K_{II}^{aux} = 1). \quad (32b)$$

4.2 Thermoelastic deformation

Coupled thermal-mechanical deformation with PD quantities are also given in PD [34, 47, 48]. Since thermoelastic deformation is addressed in Eqs. (5)-(9), thermal diffusion in PD will be briefly discussed in this part. Without considering additional heat source,

2D thermal conduction can be described by Fourier's Law as [49]:

$$\rho c_v \frac{dT_i(t)}{dt} = k \nabla^2 T_i(t), \quad (33)$$

where ρ is mass density, c_v is specific heat capacity and k is thermal conductivity. In PD, the heat conduction, without considering the effect from mechanical deformation and heat source, can be expressed as:

$$\rho c_v \dot{T}_i = \int_{H_x} \left(\tilde{\kappa} \frac{\tau}{|\xi|} \right) dV_j, \quad (34)$$

where $\tilde{\kappa}$ is micro-conductivity and τ is mean value of temperature difference between pairwise points of the bond. With the help of PDDO, the spatial PDEs in the heat conduction equation, can be replaced by integral equation directly. The transformation of material parameter between Eq. (33) and Eq. (34) becomes unnecessary. Therefore, Eq. (33) can be rewritten as:

$$\rho c_v \dot{T}_i = k \left[\int_{H_x} (T_j - T_i) g_2^{20} dV_j + \int_{H_x} (T_j - T_i) g_2^{02} dV_j \right]. \quad (35)$$

In this study, PDDO is applied in all of the simulations of thermal conduction and the calculations of interaction integral.

5 Numerical case studies

Several benchmark cases under thermoelastic effects are presented. Based on the interaction integral, single and mixed-mode static TSIFs are calculated and discussed. Results calculated by the OSPD will be validated by the reference solutions. Generally, the static numerical simulations in this study follow the procedure, which can be described by a flowchart as shown in Fig. 6. In the pre-processing part, the numerical model is defined. After discretizing the model, the horizon for each material point is established. By removing bonds or pairwise interaction, the cracks and damages on the model can be created, while the corresponding correction factors are also calculated at the same time. In the solving part, the boundary conditions are defined in each time step. Meanwhile, the PD governing equations and thermal diffusion equations are solved until the steady solutions are obtained. In post-processing part, the interaction integral with considering the thermal effect is constructed. By using PDDO, the spatial derivatives can be transformed into spatial integral terms, and hence, the evaluation of TSIFs can be implemented.

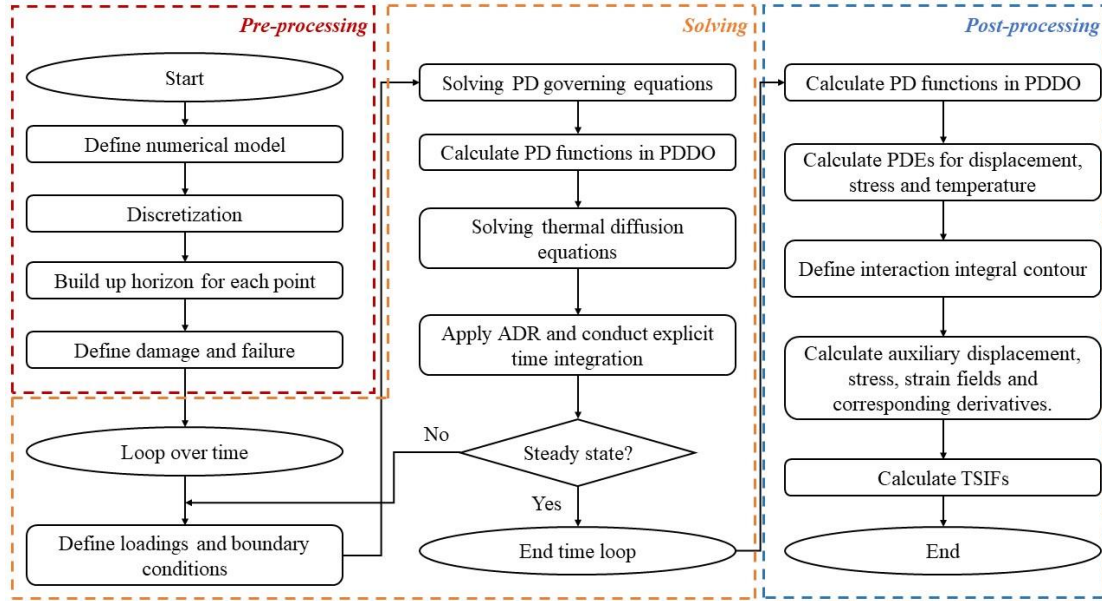


Fig. 6 Procedure of numerical simulation by OSPD

As shown in Eq. (5), the equation of motion of OSPD is in dynamic form. For static analysis, the displacement field can also be calculated by equating dynamic term $\rho \ddot{u}_i$ to 0. However, large amount of computing resource is needed, especially for problems with complex geometry, boundary condition and refined discretization. Underwood introduced a method, named as the adaptive dynamic relaxation (ADR), for static analysis [50]. By introducing a damping factor to dynamic motion, the fluctuating results will converge and the static values can be obtained. The manually defined damping factor is given in [34, 51] in detail. In this article, ADR is applied in all numerical simulations.

5.1 Isotropic plate under uniform thermal loading

Before moving to fracture analysis, it is necessary to verify the capability of OSPD in thermoelastic deformations. Therefore, a 2D intact isotropic plate is selected in this case as shown in Fig. 7. The geometrical and material properties, and loading information can be found in Table 1.

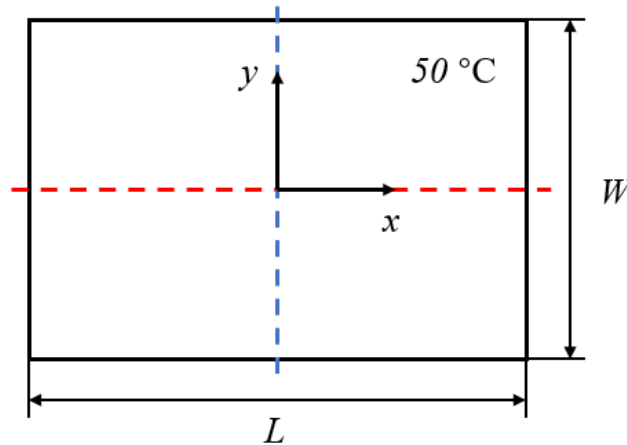


Fig. 7 Isotropic plate under uniform thermal loading

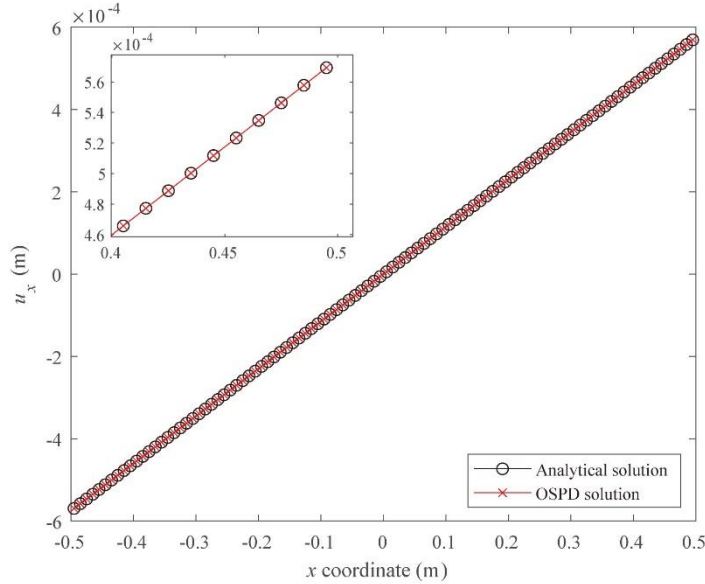
Table 1 Geometrical and material properties, and loading information of the uncracked plate

Length (m)	1.0	Poisson's ratio	1/3
Width (m)	0.5	Mass density (kg/m ³)	7,850
Thickness (m)	0.01	CTE (/°C)	2.30×10 ⁻⁵
Elastic modulus (GPa)	200	Thermal loading (°C)	50

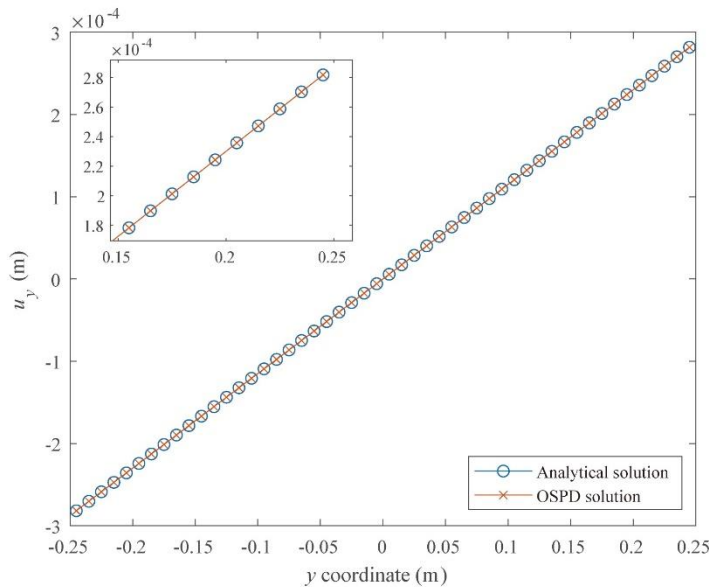
Since thickness of the plate is far less than its length and width, plane stress assumption is applied. Initially, the temperature on plate is 0 °C, and then 50 °C temperature is uniformly applied to the plate. The plate is unconstrained. The deformation of the central axes (shown as colored dash lines in Fig. 7) on the plate caused by temperature change ΔT can be obtained based on analytical solution:

$$u_x(x, 0) = \alpha \Delta T x, \quad (36a)$$

$$u_y(0, y) = \alpha \Delta T y. \quad (36b)$$



(a)



(b)

Fig. 8 Deformation along central lines: (a) u_x along horizontal axis (b) u_y along vertical axis

This case study is also investigated in [34]. However, the uniform thermal expansion is simulated by using Eq. (34) under the framework of BBPD. In this study, Eq. (35) is applied within the framework of OSPD. The plate is uniformly discretized by 100×50 material points. Fig. 8 shows the results of uniform thermal expansion. Results have showed that OSPD has strong accuracy and reliability in coupled thermal-mechanical deformation.

5.2 An edge-cracked plate under thermal loading

A strip with adiabatic edge-crack is under consideration. The strip is constrained on top and bottom surfaces. Initially, the temperature on the plate is 0°C , and then the left and right edges are subjected to low and high temperature, respectively, as shown in Fig. 9. Therefore, the plate will experience contraction on the left edge and expansion on the right edge, which will lead to a mode-I crack scenario. Geometrical and material properties, and loading information are given in Table 2. The plane strain assumption is applied.

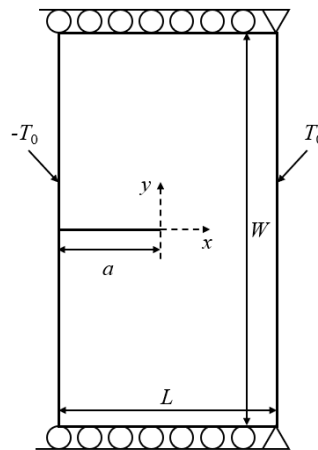


Fig. 9 An edge-cracked strip under thermal loading

Table 2 Geometrical and material properties, and loading information of the edge-cracked plate

Length (mm)	0.5	Poisson's ratio	0.25
Width (mm)	2	CTE ($^\circ\text{C}$)	1.67×10^{-5}
Crack length (mm)	0.25	Thermal loading T_0 ($^\circ\text{C}$)	1
Elastic modulus (GPa)	218.4		

The numerical simulations are implemented by ANSYS (Mechanical APDL 19.2) for FEM and MATLAB (R2020b) for OSPD. Three different uniform discretization schemes, coarse (50×200), intermediate (100×400) and refined ($250 \times 1,000$), are applied respectively. In OSPD, fictitious regions are added to the upper and lower boundaries to avoid boundary effects and provide constrains. Meanwhile, fictitious regions with a size of δ are also added on left and right boundaries. For material points located in left fictitious region, the temperature remains as -1°C , and for those located in right fictitious region, the temperature keeps at 1°C . Since the bond or pairwise interaction across the crack surface is removed, the thermal flux can not pass through the crack. Therefore, insulated boundary condition on crack surface is automatically achieved without further manual intervention. Detailed information about the fictitious

regions can be found in [34]. After reaching the static state, the crack opening displacement and corresponding temperature distribution by FEM and OSPD are shown in Fig. 10. Results show good agreement between OSPD and FEM in terms of displacement and temperature distribution.

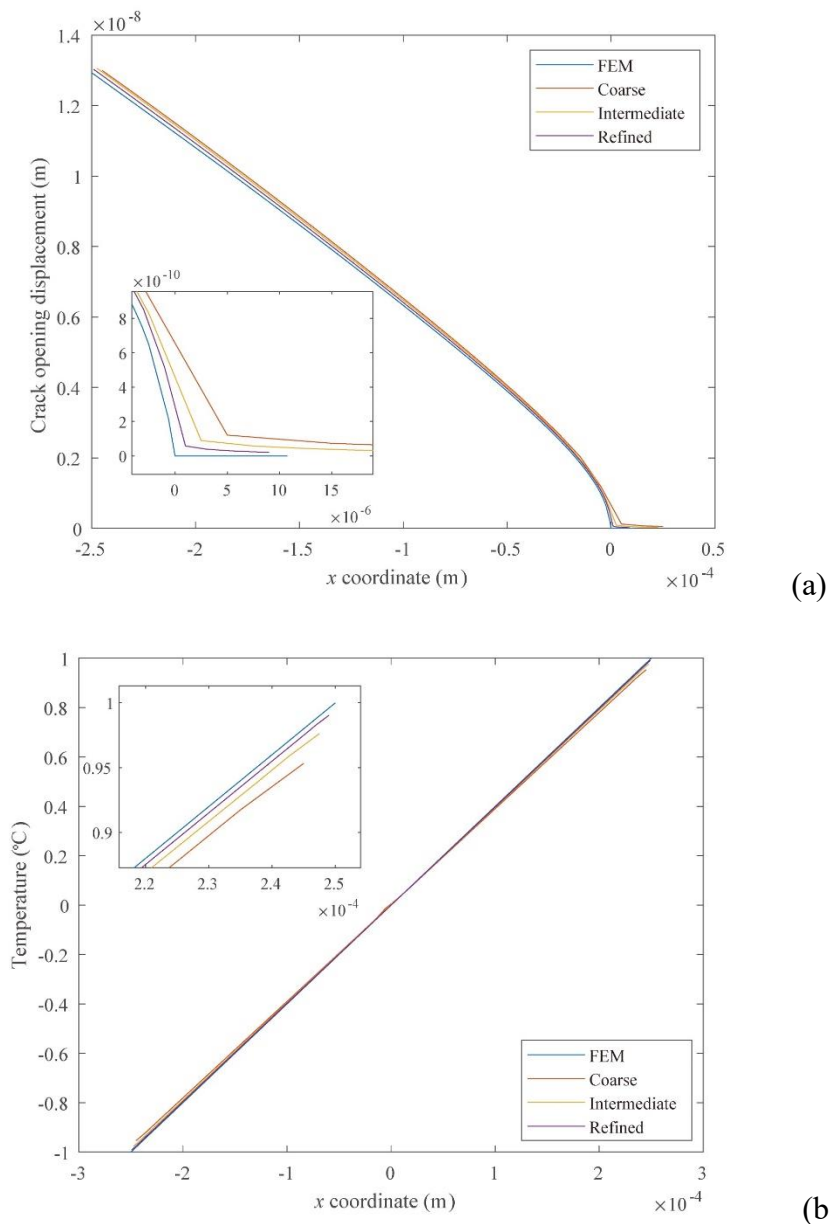


Fig. 10 Results comparison between FEM and OSPD: (a) crack opening displacement, (b) temperature distribution along crack surface

As for TSIF calculations, within the elastic deformation assumption, the mode-I TSIF is normalized as:

$$K_I^* = \frac{K_I(1 - \nu)}{E\alpha T_0 \sqrt{\pi a}}. \quad (36)$$

Static TSIF results are validated by the reference solutions, which can be found in many studies in the literatures [10, 11, 22, 52, 53]. Results by OSPD based on different integral contours are shown in Table 3.

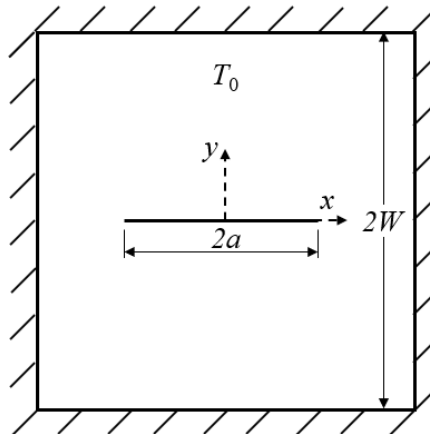
Table 3 Static TSIF results of edge-cracked plate

Coarse ($\Delta x=10^{-5}$ m)			Intermediate ($\Delta x=5 \times 10^{-6}$ m)			Refined ($\Delta x=2 \times 10^{-6}$ m)		
r_d	K_I^*	error	r_d	K_I^*	error	r_d	K_I^*	error
1.0×10^{-4}	0.535	6.90%	1.0×10^{-4}	0.532	6.48%	4.0×10^{-5}	0.497	-0.64%
1.5×10^{-4}	0.541	8.18%	1.5×10^{-4}	0.535	7.02%	8.0×10^{-5}	0.496	-0.84%
2.0×10^{-4}	0.552	10.34%	2.0×10^{-4}	0.539	7.86%	1.2×10^{-4}	0.498	-0.36%
						1.6×10^{-4}	0.501	0.24%
						2.0×10^{-4}	0.505	0.96%

Three different discretization schemes are presented in Table 3 and TSIF results are compared with reference solutions. Several integral contours are selected. Δx is grid space and r_d is the size of the integral contour as shown in Fig. 4. From the results given in Table 3, the path independency is not accomplished in coarse and intermediate discretization cases. Moreover, the accuracy of normalized mode-I TSIFs is low, as compared with reference solution. This is most likely caused by the lack of physical values due to shortage of material points. However, in refined discretization, the path independency is accomplished and the error is maintained below 1%. It has proved the reliability of OSPD in the fracture analysis under thermal loading.

5.3 A central-cracked plate under uniform thermal loading

A pre-damaged square 2D plate, with an initial temperature of 0°C , is under consideration as shown in Fig. 11. The plate is fully constrained on all boundaries. A uniform low temperature (-100°C) is applied on the plate, which leads to a global contraction of the plate. Upper crack surface moves upwards and lower crack surface moves downwards, which forms a mode-I crack scenario. Side length of the structure $2W$ is equal to 0.001 m, and a/W is equal to 0.5. Poisson's ratio is $1/3$. Other material properties of the structure remain the same as shown in Table 2. A plane stress assumption is considered.

**Fig. 11 A central-cracked plate under uniform thermal loading**

Similar to the edge-cracked case study, three discretization schemes, coarse (100×100), intermediate (200×200) and refined (400×400), are applied, respectively. Numerical results by OSPD are validated by reference solutions [54], which are shown in Table 4.

Four fictitious regions are added to all boundaries of the plate to define the boundary conditions. Within the elastic deformation assumption, mode-I SIF is normalized as:

$$K_I^* = \frac{K_I}{E\alpha|T_0|\sqrt{W}}. \quad (38)$$

Table 4 Static TSIF results of the central cracked plate

Coarse ($\Delta x=10^{-5}$ m)			Intermediate ($\Delta x=5 \times 10^{-6}$ m)			Refined ($\Delta x=2.5 \times 10^{-6}$ m)		
r_d	K_I^*	error	r_d	K_I^*	error	r_d	K_I^*	error
1.0×10^{-4}	1.306	-2.03%	1.0×10^{-4}	1.342	0.68%	5.0×10^{-5}	1.342	0.62%
1.5×10^{-4}	1.350	1.28%	1.5×10^{-4}	1.339	0.41%	1.0×10^{-4}	1.336	0.22%
2.0×10^{-4}	1.346	0.94%	2.0×10^{-4}	1.337	0.29%	1.5×10^{-4}	1.334	0.08%
						2.0×10^{-4}	1.333	-0.01%

Results calculated by the coarse case are relatively low in accuracy. However, the errors are maintained below 1% for intermediate and refined cases, which shows a good accuracy of numerical simulations. Meanwhile, path independency is also accomplished in intermediate and refined cases, which also indicates that OSPD is a reliable tool in thermoelastic fracture analysis.

5.4 A slant cracked plate under thermal loading

A 2D structure with slant crack is under investigation. Relationships between crack length and TSIFs are discussed. Initially, the temperature on the plate is defined as 0°C . High and low thermal loading are applied on upper and lower edges of the structure, respectively, as shown in Fig. 12. Meanwhile, the lower edge is fixed. Crack inclination angle ψ is equal to 30° . Length of the structure is 2.0×10^{-3} m and width of the structure is 1.0×10^{-3} m. Plane strain assumption is applied. Based on the previous TSIF studies, refined discretization scheme (400×200 or $\Delta x = 5 \times 10^{-6}$ m) is selected during the numerical implementation to keep high accuracy of numerical simulation. Two fictitious regions with size of δ are applied on the top and bottom edges. For material points located in top fictitious region, the temperature remains as 1°C . For material points located in bottom fictitious region, the temperature keeps at -1°C and displacement in y direction is fixed as 0 m. Additionally, the left corner points are fully constrained. Within the elastic deformation assumption, mixed-mode TSIFs are normalized as:

$$K_i^* = \frac{K_i}{E\alpha T_0 \frac{L}{W} \sqrt{L}} \quad (i = \text{I, II}). \quad (39)$$

Comparisons between OSPD and reference solutions in literatures [11, 53, 55] are provided in Table 6, Table 7 and Fig. 13.

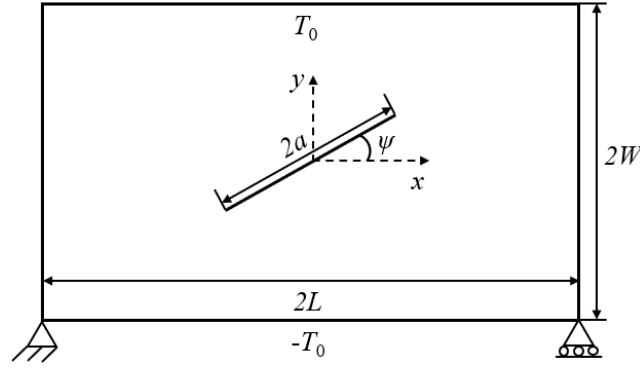


Fig. 12 Slant cracked plate under thermal loading

Table 5 Static TSIF results for $a/L = 0.3$ at $\psi = 30^\circ$

$a/L = 0.3$

r_d	K_I^*	K_{II}^*
$30\Delta x$	0.0081	0.0476
$35\Delta x$	0.0082	0.0478
$40\Delta x$	0.0084	0.0480
$45\Delta x$	0.0085	0.0481
$50\Delta x$	0.0086	0.0482

Table 6 Static TSIF results for different crack length at $\psi = 30^\circ$

	Ref. [11]		Ref. [53]		Ref. [55]		OSPD	
a/L	K_I^*	K_{II}^*	K_I^*	K_{II}^*	K_I^*	K_{II}^*	K_I^*	K_{II}^*
0.3	0.0069	0.0460	0.0060	0.0480	0.0080	0.0480	0.0081	0.0476
0.4	0.0152	0.0610	0.0140	0.0640	0.0150	0.0640	0.0154	0.0628
0.5	0.0260	0.0720	0.0260	0.0760	0.0270	0.0760	0.0258	0.0756
0.6	0.0370	0.0872	0.0400	0.0870	0.0410	0.0860	0.0386	0.0857

Table 7 Differences between reference solutions and OSPD solutions at $\psi = 30^\circ$

	Ref. [11]		Ref. [53]		Ref. [55]	
a/L	K_I^{*Ref}/K_I^*	K_{II}^{*Ref}/K_{II}^*	K_I^{*Ref}/K_I^*	K_{II}^{*Ref}/K_{II}^*	K_I^{*Ref}/K_I^*	K_{II}^{*Ref}/K_{II}^*
0.3	0.852	0.966	0.741	1.008	0.988	1.008
0.4	0.987	0.971	0.909	1.019	0.974	1.019
0.5	1.008	0.952	1.008	1.005	1.047	1.005
0.6	0.959	1.018	1.036	1.015	1.062	1.004

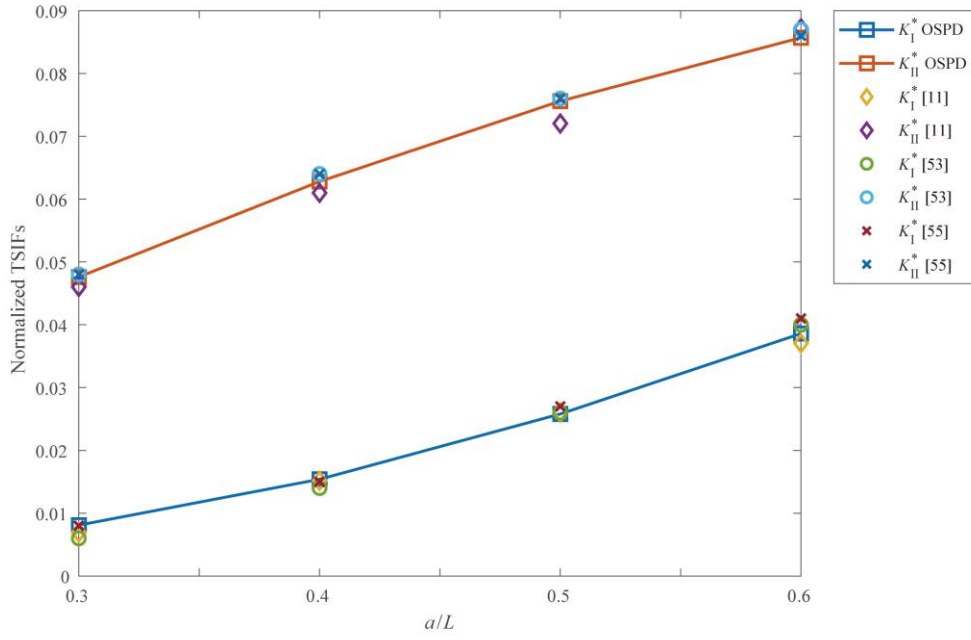


Fig. 13 Comparison of TSIFs between OSPD and reference solutions

A plate with pre-existing slant crack ($a/L=0.3$) is first selected for thermoelastic fracture analysis. Five integral contours, whose size varies from $r_d = 1.5 \times 10^{-4}$ m ($30\Delta x$) to $r_d = 2.5 \times 10^{-4}$ m ($50\Delta x$), are defined. According to Table 5, good path independency has been shown for both mode-I and -II TSIFs. Then, plate with different slant crack length is being tested. Crack size, a/L , varies from 0.3 to 0.6. Meanwhile, the size of integral contour, $r_d=1.5 \times 10^{-4}$ m ($30\Delta x$), is defined in all numerical cases. Based on loading and constrain conditions, it is a mode-II dominant situation in this case study. Therefore, mode-II TSIF is larger than the mode-I TSIF as shown in the results. As the crack length increases, the TSIFs increase as well. According to Table 6, Table 7 and Fig. 13, the OSPD solutions for different crack length vary between these reference solutions. Overall, the comparison has proved the capability in mixed-mode thermal fracture analysis.

6 Conclusion

In this study, OSPD is applied in the thermoelastic fracture analysis. As a nonlocal theory, long-range interactions are integrated within the horizon. By employing the spatial integral equation, the limitation due to geometrical discontinuity can be overcome in OSPD. Based on J-integral, interaction integral method is applied in TSIF calculation within the framework of OSPD. Meanwhile, both first and second order PDDO are utilized in thermal diffusion and TSIF calculation. PDEs are replaced by spatial integral equations, which contribute to the numerical implementations of OSPD.

Several benchmark case studies are conducted in this study. The free expansion of 2D plate under uniform thermal loading is firstly simulated. Results have proved the capability and accuracy of OSPD in analysis of thermoelastic deformation. Then mode-I TSIF is evaluated by using interaction integral. Finally, mixed-mode TSIFs are

simulated in order to investigate the relationship between crack characters and TSIFs. OSPD solutions have reached good agreements with reference solutions. It shows OSPD is a useful and reliable tool in the evaluation of TSIFs, which brings an alternative way in thermoelastic fracture analysis.

Due to the limitation of proposed method, there is relatively low accuracy in evaluation of mode-II dominant fracture problems. In future research, OSPD formulation will be optimized in order to accurately simulate the shearing behaviors of cracks. The thermoelastic fracture analysis in this article will not only contribute to the development of PD, but also provide theoretical supports for engineering practice.

Reference:

1. Irwin, G.R., Analysis of stress and strains near the end of a crack traversing a plate, *ASME Journal of Applied Mechanics*, **24**(3), 361–364 (1957)
2. Rice, J.R., A path independent integral and the approximate analysis of strain concentration by notches and cracks, *ASME Journal of Applied Mechanics*, **35**, 379-386 (1968)
3. Chen, Y.M., Numerical computation of dynamic stress intensity factors by a Lagrangian finite-difference method (the HEMP code), *Engineering Fracture Mechanics*, **7**(4), 653-660 (1975)
4. Stern, M., Becker, E.B. and Dunham, R.S., A contour integral computation of mixed-mode stress intensity factors, *International Journal of Fracture*, **12**(3), 359-368 (1976)
5. Yau, J.F., Wang, S.S. and Corten, H.T., A mixed-mode crack analysis of isotropic solids using conservation laws of elasticity, *ASME Journal of Applied Mechanics*, **47**, 335-341 (1980)
6. Yu, H., Wu, L., Guo, L., Du, S. and He, Q., Investigation of mixed-mode stress intensity factors for nonhomogeneous materials using an interaction integral method, *International Journal of Solids and Structures*, **46**(20), 3710-3724 (1980)
7. Song, S.H. and Paulino, G.H., Dynamic stress intensity factors for homogeneous and smoothly heterogeneous materials using the interaction integral method, *International Journal of Solids and Structures*, **43**(16), 4830-4866 (1980)
8. Kim, J.H. and Paulino, G.H., Consistent formulations of the interaction integral method for fracture of functionally graded materials, *ASME Journal of Applied Mechanics*, **72**(3), 351-364 (2005)
9. Zamani, A. and Eslami, M.R., Implementation of the extended finite element method for dynamic thermoelastic fracture initiation, *International Journal of Solids and Structures*, **47**(10), 1392-1404 (2010)
10. Duflot, M., The extended finite element method in thermoelastic fracture mechanics, *International Journal for Numerical Methods in Engineering*, **74**(5), 827-847 (2008)
11. Nguyen, M.N., Bui, T.Q., Nguyen, N.T. and Truong, T.T., Simulation of dynamic and static thermoelastic fracture problems by extended nodal gradient finite elements, *International Journal of Mechanical Sciences*, **134**, 370-386 (2017)

12. Hosseini-Tehrani, P., Hosseini-Godarzi, A.R. and Tavangar, M., Boundary element analysis of stress intensity factor K_I in some two-dimensional dynamic thermoelastic problems, *Engineering Analysis with Boundary Elements*, **29**(3), 232-240 (2005)
13. Reddy, J.N., *An introduction to continuum mechanics*, Cambridge University Press. (2013)
14. Hellan, K., *Introduction to Fracture Mechanics*, McGraw-Hill, New York (1984)
15. Hillerborg, A., Mod  er, M. and Petersson, P.E. Analysis of crack formation and crack growth in concrete by means of fracture mechanics and finite elements. *Cement and concrete research*, **6**(6), pp.773-781 (1976)
16. Xu, X.P. and Needleman, A. Numerical simulations of fast crack growth in brittle solids. *Journal of the Mechanics and Physics of Solids*, **42**(9), pp.1397-1434 (1994)
17. Nguyen, T.T., Yvonnet, J., Bornert, M., Chateau, C., Sab, K., Romani, R. and Le Roy, R. On the choice of parameters in the phase field method for simulating crack initiation with experimental validation. *International Journal of Fracture*, **197**(2), pp.213-226 (2016)
18. Gomez, H. and van der Zee, K.G. Computational phase-field modeling. *Encyclopedia of Computational Mechanics Second Edition*, pp.1-35 (2018)
19. Tanaka, S., Suzuki, H., Sadamoto, S., Sannomaru, S., Yu, T. and Bui, T.Q., J-integral evaluation for 2D mixed-mode crack problems employing a meshfree stabilized conforming nodal integration method, *Computational Mechanics*, **58**, 185-198 (2016)
20. Tanaka, S., Suzuki, H., Sadamoto, S., Imachi, M. and Bui, T.Q., Analysis of cracked shear deformable plates by an effective meshfree plate formulation, *Engineering Fracture Mechanics*, **144**, 142-157 (2015)
21. Tanaka, S., Suzuki, H., Sadamoto, S., Okazawa, S., Yu, T.T. and Bui, T.Q., Accurate evaluation of mixed-mode intensity factors of cracked shear-deformable plates by an enriched meshfree Galerkin formulation, *Archive of Applied Mechanics*, **87**(2), 279-298 (2017)
22. Pant, M., Singh, I.V. and Mishra, B.K., Numerical simulation of thermo-elastic fracture problems using element free Galerkin method, *International Journal of Mechanical Sciences*, **52**(12), 1745-1755 (2010)
23. Dell'Isola, F., Andreaus, U. and Placidi, L., At the origins and in the vanguard of peridynamics, non-local and higher-gradient continuum mechanics: an underestimated and still topical contribution of Gabrio Piola. *Mathematics and Mechanics of Solids*, **20**(8), 887-928 (2015)
24. Silling, S.A., Reformulation of elasticity theory for discontinuities and long-range forces, *Journal of the Mechanics and Physics of Solids*, **48**(1), 175-209 (2000)
25. Imachi, M., Tanaka, S. and Bui, T.Q., Mixed-mode dynamic stress intensity factors evaluation using ordinary state-based peridynamics, *Theoretical and Applied Fracture Mechanics*, **93**, 97-104 (2018)
26. Dai, M.J., Tanaka, S., Oterkus, S. and Oterkus, E., Mixed-mode stress intensity factors evaluation of flat shells under in-plane loading employing ordinary state-based peridynamics, *Theoretical and Applied Fracture Mechanics*, 102841 (2020)

27. Dai, M.J., Tanaka, S., Bui, T.Q., Oterkus, S. and Oterkus, E., Fracture parameter analysis of flat shells under out-of-plane loading using ordinary state-based peridynamics. *Engineering Fracture Mechanics*, **244**, p.107560 (2021)
28. Oterkus, S., Madenci, E. and Agwai, A., Fully coupled peridynamic thermomechanics, *Journal of the Mechanics and Physics of Solids*, **64**, 1-23 (2014)
29. Madenci, E. and Oterkus, S., Ordinary state-based peridynamics for thermoviscoelastic deformation, *Engineering Fracture Mechanics*, **175**, 31-45 (2017)
30. Nguyen, C.T. and Oterkus, S., Peridynamics for the thermomechanical behavior of shell structures, *Engineering Fracture Mechanics*, **219**, 106623 (2019)
31. Ren, H., Zhuang, X. and Rabczuk, T., Dual-horizon peridynamics: A stable solution to varying horizons. *Computer Methods in Applied Mechanics and Engineering*, **318**, 762-782 (2017)
32. Dorduncu, M., Borut, A. and Madenci, E., Ordinary-state based peridynamic truss element. In 56th AIAA/ASCE/AHS/ASC Structures, Structural Dynamics, and Materials Conference, 0465 (2015)
33. Silling, S.A., Epton, M., Weckner, O., Xu, J. and Askari, E., Peridynamic states and constitutive modeling, *Journal of Elasticity*, **88**(2), 151-184 (2007)
34. Madenci, E. and Oterkus, E., *Peridynamic theory. Peridynamic Theory and Its Applications*, Springer, New York, NY (2014)
35. Śolín, P., *Partial differential equations and the finite element method* (Vol. 73), John Wiley & Sons (2005)
36. Causon, D.M. and Mingham, C.G., *Introductory finite difference methods for PDEs*, Bookboon (2010)
37. Coleman, C.J., Tullock, D.L. and Phan-Thien, N., An effective boundary element method for inhomogeneous partial differential equations, *Zeitschrift für angewandte Mathematik und Physik ZAMP*, **42**(5), 730-745 (1991)
38. Cho, H.A., Golberg, M.A., Muleshkov, A.S. and Li, X., Trefftz methods for time dependent partial differential equations, *CMC-Computers, Materials & Continua*, **1**, 1-38. (2004)
39. Madenci, E., Barut, A. and Futch, M., Peridynamic differential operator and its applications, *Computer Methods in Applied Mechanics and Engineering*, **304**, pp. 408-451 (2016)
40. Madenci, E., Dorduncu, M., Barut, A. and Futch, M., Numerical solution of linear and nonlinear partial differential equations using the peridynamic differential operator. *Numerical Methods for Partial Differential Equations*, **33**(5), 1726-1753 (2017)
41. Madenci, E., Barut, A. and Dorduncu, M., *Peridynamic differential operator for numerical analysis*. Springer International Publishing (2019)
42. Wang, H., *Fracture analysis in marine batteries by peridynamic theory* (Doctoral dissertation, University of Strathclyde) (2018)
43. Wang, H., Oterkus, E. and Oterkus, S., Three-dimensional peridynamic model for predicting fracture evolution during the lithiation process, *Energies*, **11**(6), 1461 (2018)

44. Wilson, W.K. and Yu, I.W., The use of the J-integral in thermal stress crack problems, *International Journal of Fracture*, **15**(4), 377-387 (1979)
45. Fung, Y.C., *Foundations of solid mechanics* Prentice-Hall, Inc, New Jersey (1965)
46. Anderson, T.L., *Fracture mechanics: fundamentals and applications*, CRC Press (2017)
47. Silling, S.A. and Lehoucq, R.B., Peridynamic theory of solid mechanics, *Advances in applied mechanics*, **44**, 73-168 (2010)
48. Oterkus, S., Madenci, E. and Agwai, A., Fully coupled peridynamic thermomechanics, *Journal of the Mechanics and Physics of Solids*, **64**, 1-23 (2014)
49. Narasimhan, T.N., Fourier's heat conduction equation: History, influence, and connections, *Reviews of Geophysics*, **37**(1), 151-172 (1999)
50. Underwood, P., *Dynamic relaxation computational methods for transient analysis*, Elsevier Science Publishers B.V., **1**, 245–265 (1983)
51. Kilic, B. and Madenci, E., An adaptive dynamic relaxation method for quasi-static simulations using the peridynamic theory, *Theoretical and Applied Fracture Mechanics*, **53**(3), 194-204 (2010)
52. Chen, H., Wang, Q., Liu, G.R., Wang, Y. and Sun, J., Simulation of thermoelastic crack problems using singular edge-based smoothed finite element method, *International Journal of Mechanical Sciences*, **115**, 123-134 (2016)
53. Prasad, N.N.V., Aliabadi, M.H. and Rooke, D.P., The dual boundary element method for thermoelastic crack problems, *International Journal of Fracture*, **66**(3), 255-272 (1994)
54. Zhou, Z., Leung, A.Y.T., Xu, X. and Luo, X., Mixed-mode thermal stress intensity factors from the finite element discretized symplectic method, *International Journal of Solids and Structures*, **51**(21-22), 3798-3806 (2014)
55. Murkami, Y., *Stress Intensity Factor Handbook*, Pergamon Press (1987)